

## An Analytic Characterization of the Limb Asymmetry - Transit Time Degeneracy

MATTHEW M. MURPHY ,<sup>1</sup> THOMAS G. BEATTY ,<sup>2</sup> AND DÁNIEL APAI ,<sup>1,3</sup>

<sup>1</sup> *Steward Observatory, University of Arizona, Tucson, AZ, 85705, USA*

<sup>2</sup> *Department of Astronomy, University of Wisconsin–Madison, Madison, WI, 53703, USA*

<sup>3</sup> *Lunar and Planetary Laboratory, University of Arizona, Tucson, AZ, 85705, USA*

### ABSTRACT

Atmospheres are not spatially homogeneous ~~across their entirety~~. This is particularly true for hot, tidally locked exoplanets **with large day-to-night temperature variations, which can yield significant differences** between the morning and evening terminators ~~known as limb asymmetry~~. Current transit observations with the James Webb Space Telescope (JWST) are precise enough to disentangle the separate contributions of these morning and evening limbs to the overall transmission spectrum **in certain circumstances**. However, the signature of limb asymmetry in a transit light curve is highly degenerate with uncertainty in the planet's time of conjunction. As a result, literature measurements of transit times are biased if these planets have significant limb asymmetry, hindering accurate studies of limb asymmetry even with JWST. Although this degeneracy has been discussed in the literature, a general description of it has not been presented. In this work, we show how the degeneracy between limb asymmetry and the inferred time of conjunction results from apparent changes in the transit contact times when the planetary disk has asymmetric limb sizes. **We derive a general analytical formula relating the magnitude of limb asymmetry to**

the amount which it would cause the apparent time of conjunction to vary, which can reach tens of seconds for moderate levels of limb asymmetry.

When comparing our formula to simulated observations, we find that numerical fitting techniques add an additional bias to the measured time of conjunction, which results from the different occulting areas of planetary disks of differing size and shape. We also derive an analytical formula for this extra numerical bias, which is on the order of several seconds. These formulae can be applied to planning new observations or interpreting literature measurements, and we show examples for several commonly studied exoplanets.

This is a  
good abstract

## 1. INTRODUCTION

Atmospheres are not perfectly uniform ~~in nature~~. Observational surveys of brown dwarfs and planetary mass objects have found robust evidence that their atmospheres are heterogeneous and variable (e.g., Buenzli et al. 2014; Metchev et al. 2015; Apai et al. 2017). For transiting exoplanets specifically, there is abundant evidence for day-to-night variation in atmospheric temperature and cloudiness (e.g., Beatty et al. 2019; May et al. 2022, among many others) driven by the contrast in irradiation received by the day and night hemispheres. 3D atmospheric circulation models also predict that this day-to-night contrast will drive differences between the morning and evening terminator regions (e.g., Kataria et al. 2016; Line & Parmentier 2016; Powell et al. 2019), which is known as “limb asymmetry” since these terminators form the limbs of the planetary disk when seen in transit.

~~Observations~~ Observational analyses are beginning to confirm these predictions of morning-to-evening limb asymmetry. To date, most measurements of limb asymmetry have come from high spectral resolution ground-based spectroscopy, which can probe for wind speed and/or chemical abundance gradients through variable Doppler shifting between different periods of the planet’s transit (Ehrenreich et al. 2020; Bourrier et al. 2020; Hoeijmakers et al. 2020; Kesseli & Snellen 2021; Borsa et al. 2021). These observations have focused on ultra-hot exoplanets ( $\gtrsim 2100$  K), on which atomic metals like Li, Fe, and Mn (see Kesseli &

48 Snellen (2021) for an overview) are expected to be abundant and have numerous absorption  
49 lines that can only be probed at high spectral resolution. For example, Ehrenreich  
50 et al. (2020) find strong, blue-shifted iron absorption during the transit egress of WASP-  
51 76b that is not present during ingress, suggesting that gaseous iron is present in the  
52 planet’s evening terminator but not the morning terminator, implying condensation or  
53 rain-out on the cool nightside.

54 The newly launched James Webb Space Telescope (JWST) has proven capable of directly detecting  
55 limb asymmetry at low spectral resolution as well. **The observational signature of limb**  
56 **asymmetry in JWST transit observations are** apparent time of conjunction variations with  
57 wavelength (Feinstein et al. 2022; Rustamkulov et al. 2022) and changes in the spectral transit depth  
58 between ingress and egress (Murphy & et al. 2023b, in review; Espinoza & et al. 2023, in review;  
59 Delisle & et al. 2023, in review). **One advantage of JWST’s lower spectra resolution data is**  
60 **that it captures the transmission spectra, both overall and of each limb’s contribution,**  
61 **over a much wider wavelength range than is possible in high resolution spectroscopy**  
62 **from the ground. This enables more detailed retrievals of the atmospheric temperature-**  
63 **pressure structure, molecular abundances, and aerosol properties in each spatial region**  
64 **using JWST.** Extracting these separate contributions is vital to studying and understanding the  
65 circulation of heat and molecules within atmospheres. Also, previous analyses have shown that if  
66 such differences are ignored, the properties retrieved from observed data can be biased significantly  
67 from the truth (Feng et al. 2016; Caldas et al. 2019; Taylor et al. 2020).

68 One major obstacle to measuring limb asymmetry via low-resolution transmission spectroscopy is a  
69 degeneracy between the effect of limb asymmetry on the planet’s transit light curve and uncertainty  
70 in the planet’s time of conjunction. This degeneracy exists because the observable manifestation  
71 of limb asymmetry is a wavelength-dependent difference in the apparent radius of the morning and  
72 evening limbs. Not only does this alter the depth and shape of the light curve during ingress or  
73 egress, it also causes the transit to start and end slightly earlier or later. These changes in timing  
74 can be mimicked by varying the planet’s time of conjunction, which effectively translates the entire

transit slightly earlier or later in time. For example, models find that extracting limb asymmetry of approximately a scale height difference in radius requires knowing the time of conjunction to within less than one second (Line & Parmentier 2016; Espinoza & Jones 2021a). While this degeneracy has been introduced and its magnitude discussed several times in the literature (e.g. see von Paris et al. 2016; Line & Parmentier 2016; Powell et al. 2019; Espinoza & Jones 2021a), a generally applicable analytical description of the degeneracy does not yet exist. In ~~this work~~, we derive an analytical description of the degeneracy between limb asymmetry and transit timing, and compare it to commonly used numerical techniques. We believe this work will be useful for planning and interpreting observations designed to investigate limb asymmetry.

## 2. ANALYTICAL METHOD

### 2.1. Defining the problem

Consider an example planet with asymmetric limbs, where each limb is represented by a semi-circle joined to the other along its flat edge (**as in Figure 1, inspired by Espinoza & Jones 2021a,b**). The evening limb has radius  $R_{evening}$  and the morning limb radius differs by some amount  $\Delta R$ , so that  $R_{morning} = R_{evening} + \Delta R$ . This  $\Delta R$  can be positive or negative depending on which limb is larger, and herein we will assume  $\Delta R$  is positive, so that the example planet's morning limb is larger. **While this construction simplifies the geometry, we note it is not a strictly realistic model as it creates a discontinuity in the atmosphere at the planet's poles which grows with  $\Delta R$ . However, this simplified construction is likely adequate given current data quality, which we discuss later.**

An observer seeking to study this planet's limb asymmetry must measure both  $R_{evening}$  and  $R_{morning}$ <sup>1</sup> as a function of wavelength, thus constructing separate transmission spectra for each limb. **We assume that previous observers of this planet were not aware of – or not capable of – measuring limb asymmetry on the planet, and fit their data assuming the planet**

<sup>1</sup> In practice, it is really the corresponding planet-star radius ratios  $R_{evening}/R_*$  and  $R_{morning}/R_*$  that are measured from a transit light curve.

99 *had*  
 has uniform limbs. The planetary radius that these analyses will have inferred is the radius of a  
 100 uniform circle with the same occulting area – the same transit depth – as the asymmetric-limb disk,  
 101 which we call the “effective radius”  $R_{eff}$ , calculated as

$$102 \quad R_{eff} = \sqrt{\frac{1}{2} (R_{evening}^2 + R_{morning}^2)}.$$

103 Figure 1 shows a schematic of the disk of this asymmetric-limb planet, shown in blue, compared to  
 104 its uniform-limb equivalent, shown in red, at different points during transit. For reasons described  
 105 further below, these previous analyses will also have inferred a time of conjunction,  $t_{c,apparent\ uniform}$ ,  
 106 which is offset from the planet’s true time of conjunction  $t_{c,true}$  by some amount  $\Delta t_c$  due to the  
 107 planet’s limb asymmetry. In this work, we seek to understand the relationship between  $\Delta R$  and  $\Delta t_c$   
 108 and how it depends on the particular planet’s properties.

109 To best intuit the degeneracy between  $\Delta R$  and  $\Delta t_c$ , it is useful to look at the light curve of the  
 110 asymmetric-limb planet compared to its uniform-limb counterpart. Figure 1 shows an exaggerated  
 111 example of each at the bottom, which are aligned in time with the sequence of disk schematics at  
 112 the top. In this example, both planets have the exact same true time of conjunction and orbital  
 113 speed, and are moving from left to right across the stellar disk. The asymmetric-limb planet will  
 114 begin to transit before the uniform-limb planet because its leading limb, which is  $R_{morning}$ , is larger  
 115 than  $R_{eff}$ . In other words, because it has a larger limb, **the asymmetric-limb** disk makes first  
 116 contact ( $T_1$ ) with the stellar disk before the uniform-limb disk does. Similarly, since the asymmetric-  
 117 limb disks’ trailing edge,  $R_{evening}$ , is smaller than  $R_{eff}$ , it is still “ahead” of the trailing edge of the  
 118 uniform-limb disk so it will also contact the stellar disk first during the end of ingress ( $T_2$ ). The  
 119 exact same sequence of events occurs during transit egress **for the third ( $T_3$ ) and fourth ( $T_4$ )**  
 120 **contact points**. Note that even though the timing of the two transits differ, since the  
 121 planets have the same orbital speed, the duration of both transits is the same. Also note  
 122 that the shape of the ingress and egress in each light curve is slightly different due to  
 123 the different shape of each disk, but they both reach the same depth during full transit  
 124 since both disks occult the same total area.

maybe we just use  
"apparent" ?

is there a  
more  
(1)  
concise  
name to  
use here?

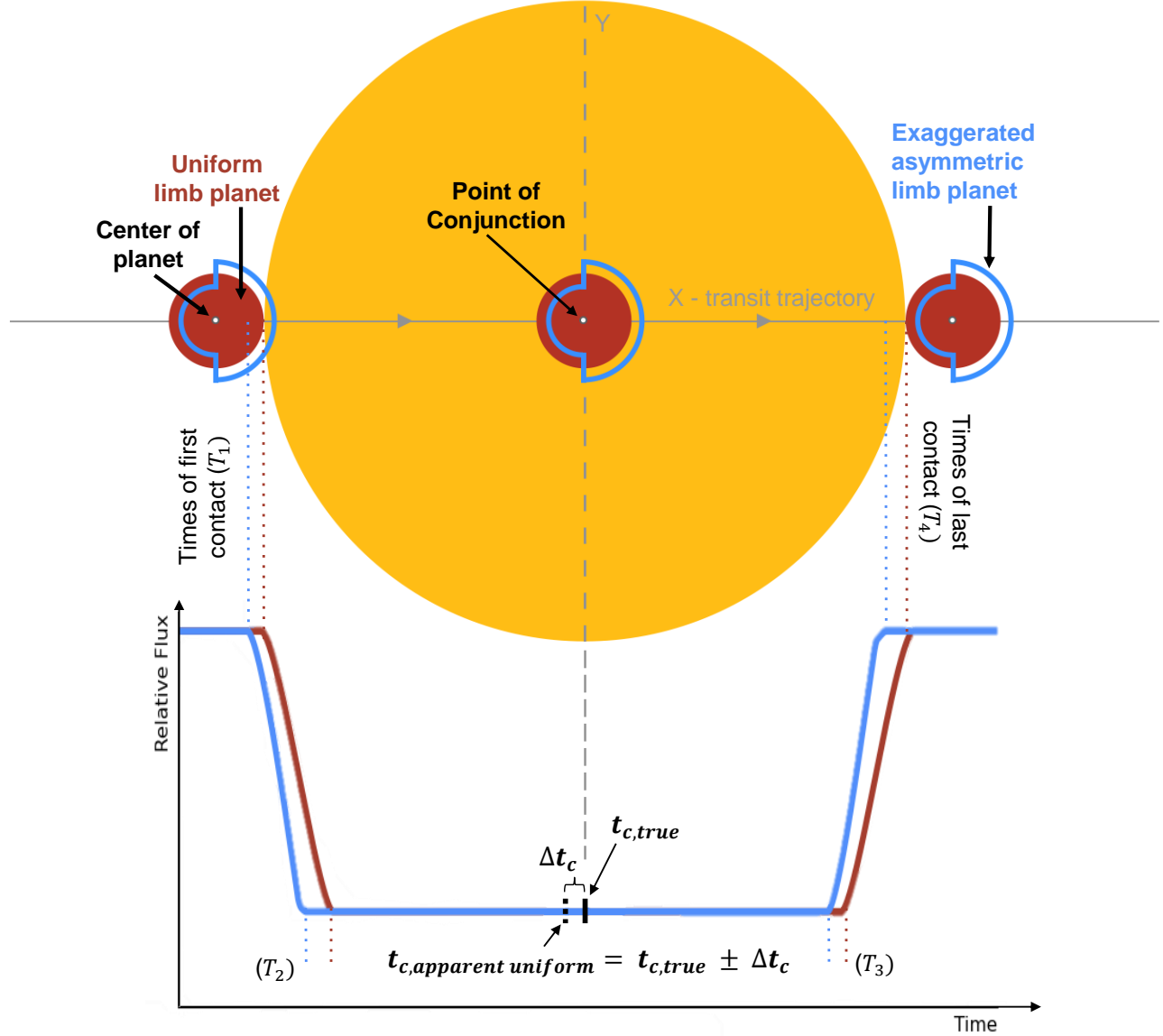


**Figure 1.** Exaggerated schematic illustrating the difference in the transit light curves of an asymmetric-limb planet and a uniform-limb planet. Both planets share the same time of conjunction. Due to the difference in their leading and trailing limb radii though, the transit contact times of each planet differ. An observer that measures the light curve of the asymmetric limb planet, which is shown in blue, and fits their data using a uniform-limb transit model would infer a biased time of conjunction because these changes in the contact times effectively shift the transit earlier or later in time. This is the origin of the degeneracy between limb asymmetry and variations or uncertainty in a planet's time of conjunction.

Even though the two planets in Figure 1 have the same true time of conjunction, they have different contact times ( $T_1 - T_4$ ) due to the difference in their limb radii, **and this results in** an apparent shift in the transit light curve along the time axis. That is, the blue light curve (of the asymmetric-limb planet) in Figure 1 looks like the red light curve (of the uniform-limb planet) but shifted slightly earlier in time. **Using our notation**, this means the uniform-limb planet’s apparent time of conjunction  $t_{c,apparent\ uniform}$  is shifted slightly earlier by an amount  $\Delta t_c$ .

**This apparent shift in time** is the source of the degeneracy between limb asymmetry and transit timing: the changes in the transit contact times due to limb asymmetry can be mimicked by varying the transit’s time of conjunction and keeping the limb radii equal. **The consequence for an observer is that while the blue light curve is the underlying astrophysical reality, literature analyses that do not account for potential limb asymmetry will infer the planet’s time of conjunction to be  $t_{c,apparent\ uniform}$  rather than  $t_{c,true}$ .** This presents a problem, because even if an observer obtains an ultra-high-precision light curve, if they fix the time of conjunction to  $t_{c,apparent\ uniform}$  in their model they will not detect any limb asymmetry. Its effect has been canceled out by the systematic error ( $\Delta t_c$ ) in the assumed transit time.

In the next section, we will derive a description for this degeneracy by solving for the relation between  $\Delta R$  and  $\Delta t_c$ . We take advantage of the fact that, for a circular orbit in the uniform-limb case, the first and last contact times are equidistant from the time of conjunction. As a result, we can transform translations in  $t_c$  to translations in  $T_1$  and  $T_4$  which can be geometrically related to the shape and size of the planetary disk. In essence, we are solving the problem of what  $\Delta t_c$  is necessary to make the  $T_1$  and  $T_4$  of the uniform-limb light curve be the same as those of the asymmetric-limb light curve.

## 2.2. Times of first and last contact

We assume that each planet rotates about a single axis which is oriented parallel to its orbital axis and lies in the plane of the page. As shown in Figure 1, we construct each planetary disk as two semi-circles whose straight edges are joined along the planet’s rotation axis. Here, we explicitly define the “center” of each planet as the point where the

152 rotation axis meets the two lines which bisect the arcs of each semi-circle, as indicated  
 153 in Figure 1. Under this construction, these bisectors are parallel to the planets' transit  
 154 trajectories. To aid our derivation, we will work in a cartesian coordinate system as is also shown  
 155 in Figure 1. The x-axis is aligned along the planet's transit chord, so that the center of the planet is  
 156 always moving directly along the x-axis.

157 **The point of conjunction is the position of the center of each planet at its time of**  
 158 **conjunction, defined as when each planet is exactly midway in space (i.e., in  $x$ ) between**  
 159 **the points where its center crosses the stellar disk during ingress and egress. We define**  
 160 **this point of conjunction to be the origin of our coordinate system, so that the y-axis**  
 161 **passes through this point and is orthogonal to both planets' transit trajectories. Note**  
 162 **that in Figure 1, we assume both planets transit directly along the stellar equator but**  
 163 **this need not be true in general. Our coordinate system is invariant to general changes**  
 164 **in the planets' orbital orientations as the x-axis can be translated vertically along the**  
 165 **stellar disk and the y-axis rotated such that the x-axis is always horizontal.**

166 We assume the planets are of identical mass, which is negligible compared to the mass of the star,  
 167 and are on identical circular orbits with semi-major axis  $a$  and period  $P$ . The tangential speeds of  
 168 each planet in their orbit are thus equal and given by

$$v_p = \frac{2\pi a}{P}. \quad (2)$$

170 Since these orbits are circular,  $v_x \leq v_p$  as some motion is directed in the radial direction  
 171 except at the point of conjunction. For simplicity, however, we will make the assumption that  
 172  $v_x = v_p$  as this correction is generally small enough that it can be neglected.

When the asymmetric-limb planet makes first contact, assuming it has a larger leading limb, the uniform-limb planet will still need to travel some extra projected distance in the x-direction before it too makes first contact. Let us hold the asymmetric-limb planet fixed at first contact, and let the uniform-limb planet move forward in time until it too makes first contact. Then, we solve for the difference in these times via this extra projected distance  $\Delta x$  that the uniform-limb planet travels.

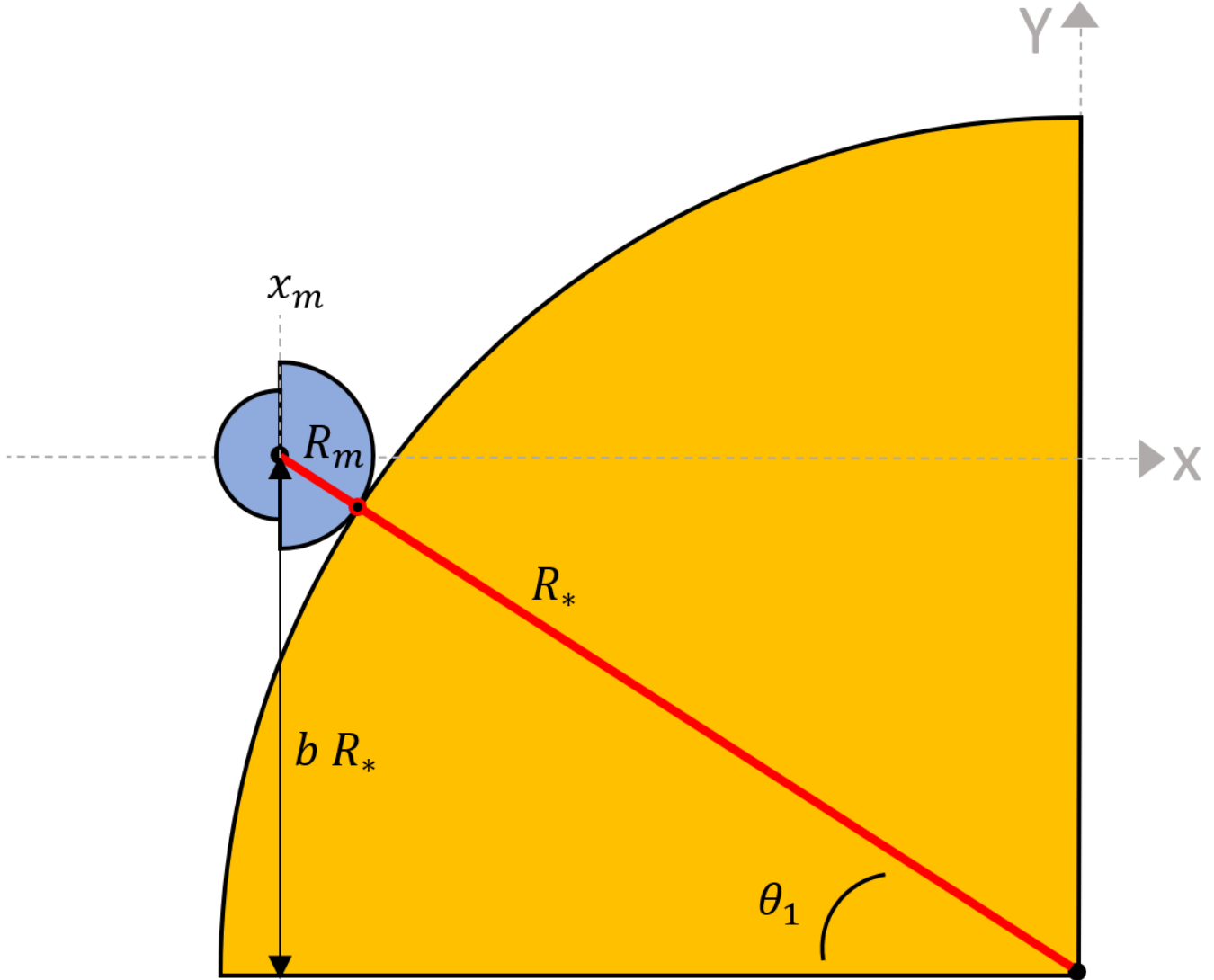


**Figure 2.** Projected geometry of a planet with asymmetric limbs at transit first contact. A line can be drawn from the center of the star to the center of the planet which passes through the point of first contact. This line defines the hypotenuse of a triangle which we use to derive how the time of first contact changes as the leading limb radius changes in Equation 9.

When the planets are transiting along the stellar equator, as is shown in Figure 1, this is simply  $\Delta x = R_{morning} - R_{eff} \approx \Delta R/2$ . **For non-zero impact parameters, estimating  $\Delta x$  is more involved.** Figure 2 shows the projected geometry at the point of first contact for an asymmetric-limb planet with non-zero impact parameter. We can draw a triangle **with a hypotenuse** from the center of the stellar disk, through the point of first contact, to the center of the planetary disk. The length

of this hypotenuse is  $R_\star + R_{morning}$  and it makes an angle  $\theta_1$  with respect to the stellar equator. The projected vertical distance between the center of the planet and the stellar equator is  $bR_\star$ , where  $b$  is the impact parameter. Let us define the position of the center of the asymmetric-limb planet when its leading limb makes first contact as  $x_m$ , and likewise for the uniform-limb planet as  $x_u$ . The extra distance travelled by the uniform-limb planet is

$$\begin{aligned}\Delta x &= x_m - x_u \\ &= (R_m + R_\star) \cos(\theta_{1,asym.}) \\ &\quad - (R_{eff} + R_\star) \cos(\theta_{1,unif.}).\end{aligned}\tag{3}$$

<sup>173</sup> For the triangle constructed in Figure 2, we can write

$$\sin(\theta_{1,i}) = \frac{bR_\star}{R_\star + R_{p,i}}.\tag{4}$$

<sup>175</sup> Here,  $R_{p,i}$  can be  $R_{morning}$  or  $R_{eff}$ . We can convert Equation 4 to the cosine of the angle,

$$\cos(\theta_{1,i}) = \sqrt{1 - \left(\frac{bR_\star}{R_\star + R_{p,i}}\right)^2},\tag{5}$$

<sup>177</sup> and thus

$$x_i = (R_\star + R_{p,i}) \sqrt{1 - \left(\frac{bR_\star}{R_\star + R_{p,i}}\right)^2}\tag{6}$$

$$= \sqrt{(R_\star + R_{p,i})^2 - (bR_\star)^2}.\tag{7}$$

<sup>180</sup> We can then rewrite Equation 3 as

$$\Delta x = \sqrt{(R_\star + R_m)^2 - (bR_\star)^2} - \sqrt{(R_\star + R_{eff})^2 - (bR_\star)^2}.\tag{8}$$

In the limiting case of  $b = 0$ , this simplifies back to  $\Delta x = R_m - R_u$ . Then, since  $\Delta T_i = \Delta x / v_p$ , the difference in the times of first contact is

$$\Delta T_1 = \frac{P}{2\pi a} \left( \sqrt{(R_\star + R_{morning})^2 - (bR_\star)^2} - \sqrt{(R_\star + R_{eff})^2 - (bR_\star)^2} \right).\tag{9}$$

The same derivation can be done for the time of fourth contact by swapping the morning limb radius for the evening limb radius. In our construction, the uniform-limb planet will also make

fourth contact after the asymmetric-limb planet, now because the uniform-limb radius is larger than the evening-limb radius. Changing out terms, we then have

$$\Delta T_4 = \frac{P}{2\pi a} \left( \sqrt{(R_\star + R_{eff})^2 - (bR_\star)^2} - \sqrt{(R_\star + R_{evening})^2 - (bR_\star)^2} \right). \quad (10)$$

By construction,  $\Delta T_1$  and  $\Delta T_4$  will always have the same sign. This is because the equivalent-depth uniform radius will always be between the two limb radii, so  $T_1$  and  $T_4$  will always be earlier or later together. If the asymmetric-limb planet's morning limb is larger than its evening limb, as we have been using in our constructed example, then  $\Delta T_1$  and  $\Delta T_4$  will be negative. If the evening limb is larger, then they will be positive. Then, because these contact times are equidistant about the time of conjunction for the uniform-limb planet,

$$\Delta t_c = \frac{1}{2} (\Delta T_1 + \Delta T_4). \quad (11)$$

182

### 3. NUMERICAL METHOD

183

#### 3.1. Setup

*move the bolded clause to the 2nd part of the sentence*

To compare our analytic formulae in Section 2.2 to the effect as simulated by state-of-the-art numerical models, we simulated transit observations of the exoplanets WASP-107b, WASP-39b, WASP-96b, and WASP-80b. We chose these specific planets because they span a wide range of bulk atmospheric scale heights, which we use as a measure of the magnitude of limb asymmetry. For these simulations, we collected literature values for several planetary and orbital parameters, which are listed in Table 1. We computed a bulk atmospheric scale height  $H$  of each planet based on the published mass, radius, and equilibrium temperature, and an assumed atmospheric mean molecular weight of 2.3 atomic mass units for each planet. We then followed our previous construction by setting the planet's evening limb radius  $R_{p,evening}$  to the published radius, then compute the morning limb radius as

$$R_{p,morning} = R_{p,evening} + N \times H. \quad (12)$$

184

Here,  $N$  is any positive number and  $N \times H$  takes the place of  $\Delta R$  so that the radii of the evening and morning limbs differ by some multiple of the planet's bulk scale height.

185

We then simulated one transit observation of each planet. We first generated a model light curve of the asymmetric-limb planet using the transit modeling package `catwoman` (Jones & Espinoza 2022; Espinoza & Jones 2021b) with literature values for the orbital parameters, the above prescription for the limb radii assuming some value for  $N$ , and assuming the axis separating the limbs is aligned to the orbital axis. We use this model light curve as a reference for generating synthetic observed data, computing the relative flux value of each synthetic data point as as

$$y_{data,i} = y_{model,i} + \mathcal{G}(\mu = 0, \sigma). \quad (13)$$

Here, we emulate photon noise in the light curve by adding pure white noise to these data via the function  $\mathcal{G}(\mu = 0, \sigma)$ , which represents draws from a Gaussian distribution with a mean of zero and a standard deviation of  $\sigma$ . We assume this photon noise is the only source of scatter in the light curve.

We first simulated a “perfect” transit observation of the exoplanet WASP-39b in order to directly compare to our analytical formulae. We placed data points at a cadence of 0.5 seconds and used an effectively negligible light curve scatter ( $\sigma$ ) of only 1 part-per-million. For this “perfect” observation, we finely sampled  $N$  in twenty evenly-spaced steps between 0 and 5.

We then simulated more realistic transit observations of each planet using the optimal integration cadences computed using PandExo (Batalha et al. 2017) for a JWST/NIRCam F322W2 observation, and light curve scatters of 200 ppm. These computed cadences are given in Table 1 and ranged from  $\sim$ 15 - 80 seconds. For these simulations, we used a coarser sampling for  $N$  of ten steps between 0 and 5. For WASP-96b, its nominal cadence of 144 s and 200 ppm light curve scatter led to large noise in our simulation results. We therefore used a  $2\times$  faster cadence of 72 s and slightly smaller scatter of 150 ppm just for WASP-96b, which did not change the underlying result but made it easier to visually present and compare to our analytical results. In all cases, we assumed having an equal time out-of-transit baseline to the published transit duration.

*→ how do these compare to what you'd get in real life?*

211 After generating the simulated observed data, we fit these data using a uniform-limb transit model  
212 generated by the transit modelling package `batman` (Kreidberg 2015). We left all parameters fixed  
213 to their true values except for the time of conjunction, which was allowed to vary freely. We set  
214 the planetary radius to the value which would have the same planetary disk occulting area as the  
215 corresponding asymmetric-limb disk, using [equation 1](#). We fit the data using the Markov Chain Monte  
216 Carlo method using `emcee` (Foreman-Mackey et al. 2013), sampling just the time of conjunction for  
217 5,500 steps which was more than sufficient for each run’s sampling to converge.

218 We chose to use uniform limb darkening when generating the reference light curves, meaning the  
219 stellar disks are completely uniform in brightness. This choice was partially motivated by computa-  
220 tional efficiency, as the overhead initializations of `catwoman` and `batman` are significantly slower when  
221 limb darkening must be computed. It was also motivated by our desire to treat each planet uniformly,  
222 as different host stars exhibit different limb darkening that may yield different results depending on  
223 the assumed cadence or noise of the light curve. We did test various limb darkening laws, including  
224 quadratic and logarithmic, and various sets of limb darkening coefficients. We found that the precise  
225 choice of limb darkening did not change our result because we set the limb darkening when generating  
226 the reference light curve and kept it fixed for all later steps, thus assuming perfect knowledge of limb  
227 darkening during the light curve fitting. Uncertainty in the limb darkening coefficients is of concern  
228 to real observations, but is beyond the scope of our analysis and can be mitigated using stellar models  
229 in practice.

### 230 3.2. *Connection to literature measurements*

231 Our numerical method described in Section 3.1 resembles the method by which most, if not all,  
232 literature measurements of exoplanet transit times are determined. In reality, one obtains a transit  
233 observation of an exoplanet which may or may not have asymmetric limbs. The data is then typically  
234 fit using a uniform-limb model, using `batman` or similar light curve models, typically using a Bayesian  
235 parameter sampling technique, such as `emcee`. Therefore, using this numerical method we are able  
236 to directly compare our analytical predictions to what one may **derive** from a real observation,

*specify this is for the planet.  
After the LD discussion above, it took  
me a second.*

**Table 1.** Planetary and Stellar Properties used in our Transit Observation Simulations

Parameter [units]	WASP-80 b	WASP-96 b	WASP-39 b	WASP-107 b
P [days]	3.06785271(19) <sup>a</sup>	3.4252565(8) <sup>a</sup>	4.0552941(34) <sup>f</sup>	5.721488(3) <sup>a</sup>
$a / R_s$	$12.63 \pm 0.13^b$	$9.03 \pm 0.30^d$	$11.55 \pm 0.13^g$	$18.2 \pm 0.1^j$
$i$ [degrees]	$89.02 \pm 0.11^a$	$85.6 \pm 0.2^c$	$87.32 \pm 0.17^f$	$89.7 \pm 0.2^j$
$R_p / R_\star$	0.17137(39) <sup>a</sup>	0.1186(17) <sup>d</sup>	0.1457(15) <sup>h</sup>	0.14434(18) <sup>k</sup>
$R_\star [R_\odot]$	$0.605 \pm 0.048^*$	$1.15 \pm 0.03^*$	$0.92 \pm 0.03^*$	$0.73 \pm 0.15^*$
$M_p [\text{M}_{\text{Jupiter}}]$	$0.538 \pm 0.035^a$	$0.49 \pm 0.04^e$	$0.281 \pm 0.032^f$	$0.096 \pm 0.005^l$
$T_{eq}$ [K]	$825 \pm 19^a$	$1285 \pm 40^c$	$1166 \pm 14^f$	$770 \pm 60^j$
$T_{14}$ [hours]	$2.131 \pm 0.003^a$	$2.4264 \pm 0.0264^c$	$2.8032 \pm 0.0192^i$	$2.753 \pm 0.007^j$
$\mu$ [amu]	2.3	2.3	2.3	2.3
H [km]	$226 \pm 44$	$669 \pm 97$	$1042 \pm 171$	$1221 \pm 174$
Cadence [s]	14.8	72.0	79.5	20.2
$\sigma$ [ppm]	200	150	200	200

References—<sup>a</sup>Kokori et al. (2022), <sup>b</sup>Triaud et al. (2015), <sup>c</sup>Hellier et al. (2014), <sup>d</sup>Patel & Espinoza (2022), <sup>e</sup>Bonomo et al. (2017), <sup>f</sup>Mancini et al. (2018), <sup>g</sup>Fischer et al. (2016), <sup>h</sup>Maciejewski et al. (2016), <sup>i</sup>Faedi et al. (2011), <sup>j</sup>Anderson et al. (2017), <sup>k</sup>Dai & Winn (2017), <sup>l</sup>Piaulet et al. (2021), <sup>\*</sup>Gaia

Don't center-align the references or note text

NOTE—Uncertainties with many digits are given in parenthetical form, where the values of N digits in each parenthesis replace the last N significant digits of the measured value. For example, 0.03(1) means  $0.03 \pm 0.01$ . Values without associated references were either assumed or calculated based on other values.

Parameter definitions:  $P$  = orbital period,  $a$  = semi-major axis,  $R_\star$  = stellar radius,  $i$  = orbital inclination,  $R_p$  = planetary radius,  $M_p$  = planetary mass,  $T_{eq}$  = planetary equilibrium temperature,  $T_{14}$  = transit duration,  $\mu$  = bulk mean molecular weight,  $H$  = bulk atmospheric scale height, Cadence = synthetic observation data cadence,  $\sigma$  = synthetic observation light curve scatter.

and thus evaluate any inconsistencies between them which would have implications for literature measurements.

### 3.3. Comparing our analytical and numerical results

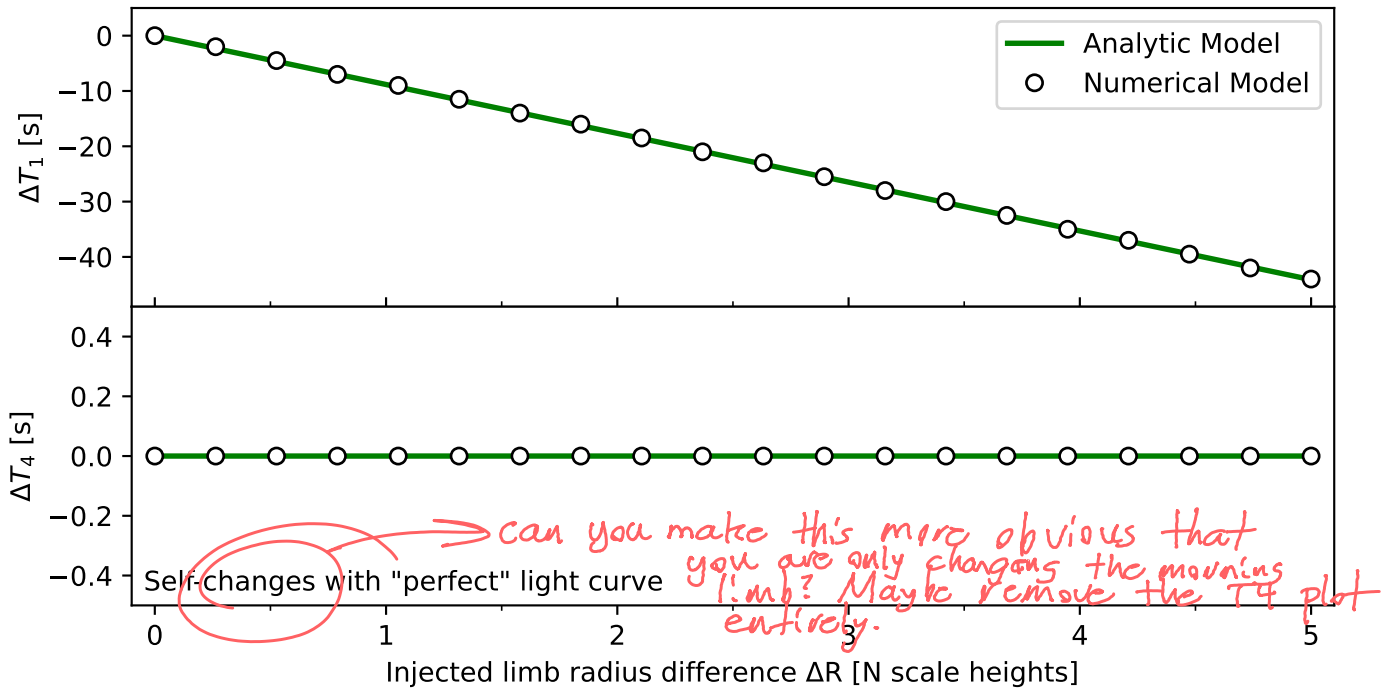


**Figure 3.** Changes in the time of first ( $\Delta T_1$ ) and last ( $\Delta T_4$ ) contact due to extending the radius of our example planet’s morning limb relative to the evening limb. We defined this radius extension  $dR$  in multiples of the planet’s atmospheric scale height, as given on the x-axis. For this example, we used literature parameters for the planet WASP-39b and generated light curves using the transit model `catwoman` for each  $dR$ . Then, we recorded how  $T_1$  and  $T_4$  of each light curve changed relative to the case of uniform limb sizes (i.e.  $dR = 0$ ), shown as the black points. We compare these results to our analytical predictions for  $\Delta T_1$  and  $\Delta T_4$ , given in Equations 9 and 10, which we find perfectly predict the numerical results.

240 First, we recorded the reference light curves generated for the “perfect” observation, determined the  
 241 first ( $T_1$ ) and last ( $T_4$ ) contact times of each light curve, and calculated the change in both relative  
 242 to the  $N = 0$  (i.e. uniform-limb) case as  $N$  increased. **We compared these changes to what**  
 243 **Equations 9 and 10 predict and find they perfectly agree, which is shown in Figure 3.** In  
 244 terms of magnitude, we find that  $T_1$  occurs over 40 seconds earlier when the morning limb radius is  
 245 increased by 5 scale heights. Note that the time of last contact does not change because it depends  
 246 on changes in the evening limb radius which we kept fixed. Also, we remind the reader that these  
 247 light curves were generated using WASP-39b’s orbital parameters which is an inclined orbit, thus  
 248 verifying that Equations 9 and 10 indeed handle general orbits well.

→ see comment above. You could just phrase  
 this as an exercise in changing the morning  
 and  $T_1$

next computed the difference between

Okay, I guess you need both for  $T_c$ . Still, I'd make it more clear in the plot about what's up w/  $T_c$

Then, we compared the best-fit time of conjunction of the uniform-limb model on the "perfect" observation's simulated data to the true value, which is  $\Delta t_c$ , shown as the circular points in Figure 4. We compared this numerical result to our analytical model's prediction for  $\Delta t_c$  from Equation 11, shown as the blue line. We find that our simulated fit finds a larger  $\Delta t_c$  than is predicted by a factor of about 10% at all  $N$ , reaching nearly a three second discrepancy at our maximal case of limb asymmetry of  $N = 5$ . Through trial and error, we found that this discrepancy consistently appeared, with approximately the same relative magnitude, regardless of our specific choice of planetary parameters, limb darkening coefficients, noise parameters, etc., leading us to discover that there is an underlying physical mechanism in all of our numeric vs. analytic comparisons. I'd like to keep some kind of "promise" of a solution later on, so which we explain in the next section. that the reader doesn't read we have a problem, and stop there.

### 3.4. Extra-area compensation when fitting transits

the time offsets estimated by our numerical model

The discrepancy between our numerical simulation result and our analytical model, as shown in Figure 4, stems from an inherent difference in what each aims to measure. Our analytical formula was derived to specifically calculate the  $\Delta t_c$  required to make the  $T_1$  of the asymmetric-limb and uniform-limb planets match. In the numerical method, we are instead calculating the "best-fit"  $t_c$  of the uniform-limb model when it is applied to the data generated from an asymmetric-limb model. The "best-fit" solution is determined not strictly by making the  $T_1$  values match, but by the specific value of the parameter that optimizes the goodness-of-fit metric used by the fitting routine. In our case, this metric was the Bayesian likelihood. We find that our discrepancy results from an overcompensation in  $\Delta t_c$  by the numerical sampling which, due to the geometry of the planetary disks, better minimizes the residuals in the fits to our simulated data.

We illustrate how this extra-area compensation effect arises in Figure 5. The planetary disks represented by our model light curves are shown for reference in panel A, with the uniform-limb planet's disk in red and the asymmetric-limb planet's disk in blue. Panels B, C, and D represent the planet approaching transit, with the star represented as the uniform yellow-orange disk. We start

Structurally, you need to make those match in the text, Numeric vs analytic model, not numeric method vs analytic model

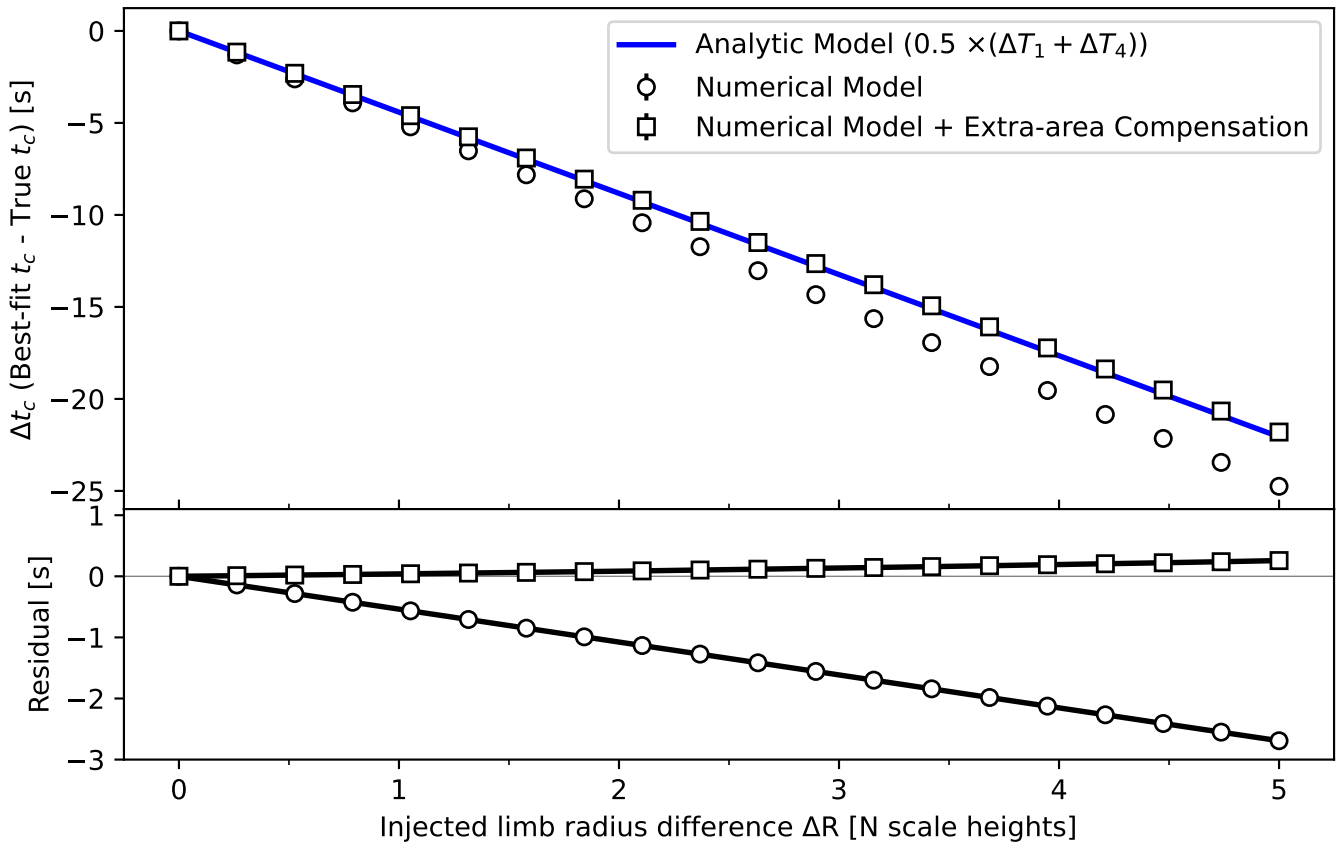


**Figure 4.** Measured times of conjunction compared to the true times of conjunction, as a function of the injected difference in radius between the planet's evening and morning limbs. The circular points show our nominal numerical results obtained from fitting a synthetic observation of WASP-39b with ideal cadence and light curve scatter, where the data is generated around an asymmetric limb transit model but fit using a uniform-limb transit model. The blue line shows our analytical model's prediction for this bias in  $t_c$  from Equation 11, derived from the extra distance that a uniform-limb disk with the originally same  $t_c$  as an asymmetric-limb disk needs to travel before they have the same first and last transit contact times. We find a discrepancy between this analytical prediction and the result of our simulated observations (circular points) which is due to the numerical extra-area compensation effect, described in Section 3.4. The square points show the numerical results when including this compensation effect, derived in Equation 18, which we see brings the two models into agreement.

276 by treating the planets as having the same  $t_c$ , shown in panel B. In panel C, we proceed to the time  
 277 when the asymmetric-limb planet makes first contact with the stellar disk. Nominally, when the two

planets have the same  $t_c$ , the uniform-limb planet would not yet be making first contact but would take some extra time  $\Delta t_c$  before it does. Our analytic formula solves for  $\Delta t_c$  so as to make both planets make first contact at exactly the same time, as is illustrated in panel C. In this arrangement, however, the asymmetric-limb planet has two regions of "extra" occulting area due to its larger leading limb which are indicated by the blue arrows. During the first half of transit ingress, these regions of extra occulting area will lead to the asymmetric-limb planet having larger transit depth and a steeper ingress slope, thus causing a large residual between the two planets' light curves despite them making first contact at the exact same time. The numerical approach disfavors this arrangement as a solution due to this large residual, hence it finds a different solution. As we see from the residuals in Figure 4, the numerical approach prefers an even larger  $\Delta t_c$  which is equivalent to moving the uniform-limb planet even further to the right in our schematic. This favored numerical solution is illustrated in panel D, where the uniform-limb planet now has  $\Delta t_c + \tau$ , where  $\tau$  represents the extra timing bias compensated by the numerical approach. This arrangement is preferred by the numerical approach because, as a result of the uniform-limb planet now being slightly ahead of the asymmetric-limb planet, the uniform-limb planet now has some extra occulting area at the leading edge of its disk as indicated by the red arrow. This red-arrow area effectively cancels out the blue-arrow areas, and an equivalent effect happens with the trailing disk edges. As a result, neither disk has net excess occulting area, leading to a minimized residual between their light curves during ingress and egress.

We derive an analytical formula for this extra-area compensation  $\tau$  by considering the extra path length required to be traveled by a planet with increased hemisphere radius during ingress before that hemisphere becomes fully internally tangent. Figure 6 sketches this situation, where we have aligned the uniform-limb and asymmetric-limb disks from our schematic in Figure 5 such that they are concentric (i.e. share the same  $t_c$ ) and are positioned where the center of the planet contacts the stellar disk. Note that we have folded the asymmetric-limb planet so that both of its hemispheres are entering transit for illustration purposes. As before, each planet's motion is purely along the x-axis as time progresses. At this point in time, each planet still has extra area in the bottom right which is yet to occult the star. Therefore, each disk must still travel a certain distance until its

*let's talk about this P*

*explain why in like 1 sentence*

*top left of Fig 6*

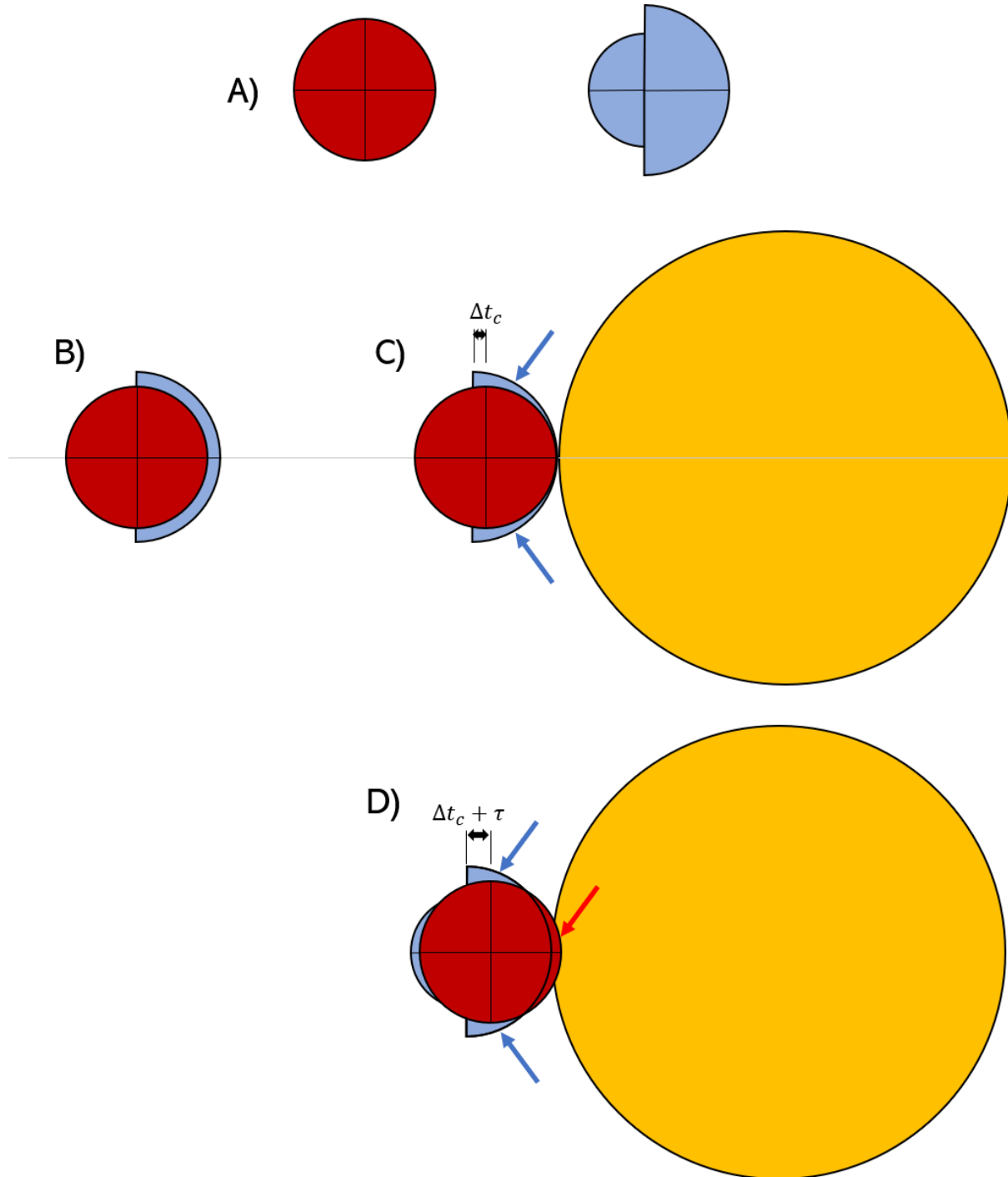


**Figure 5.** Schematic of the extra-area compensation problem. Panel A shows the uniform-limb disk in red, which is used in the model being fit to the synthetic data generated based on the asymmetric-limb disk, which is shown in blue. These two model planets are initially set to have the same time of conjunction  $t_c$ , in which case their disks are overlaid as in Panel B. Due to limb asymmetry imprinted into the data, this fit will return a biased  $t_c$  when using this uniform-limb model. Panel C shows our analytic solution for how much this bias ( $\Delta t_c$ ) will be, derived from the extra distance that the uniform-limb disk needs to travel along the transit trajectory until its first (and last) contact times are the same as for the asymmetric-limb disk. The extra occulting area of the asymmetric-limb disk in this arrangement, indicated by the blue arrows, leads to a large fitting residual and thus is disfavored by our numerical fit. Rather, the numerical fit prefers

*just say  
the top of the disk*

*is there a less technical term  
you can use? "Fully on the disk?"*

*edge of the*

polar point – the edge of the disk on the y-axis – also contacts the stellar disk edge at which point the shown hemisphere would become fully internally tangent. This length is equal to a line drawn from the polar point to the the edge of the stellar disk, represented as the thick black curve, at the same y. We shows an example for the asymmetric-limb planet's larger morning hemisphere as the orange points and orange connecting line. In the coordinate system shown in Figure 6, the length of this line is just equal to the x-value of the curve defining the stellar disk edge as a function of y. The stellar disk is a uniform circle of radius  $R_\star$  and is centered at  $y=0$ ,  $x=R_\star$  in these coordinates, so its disk edge is defined by

$$y^2 + (x - R_\star)^2 = R_\star^2 \quad (14)$$

which can be solved for x to give

$$x = R_\star - \sqrt{R_\star^2 - y^2}.$$

*which  
↑ curve?*

Note that x and y are both distances in this equation. This full x-length is not needed, however. By the time the planet has traversed approximately  $x/2$ , an equal area to what remains below the curve will have appeared above the curve. This represents the condition of achieving the mutually canceling make less technical occultation areas that we illustrated in panel D of Figure 5, and is what defines the magnitude of the resulting over-compensation. This compensation  $\tau$  is then related to the difference in  $x/2$  between the uniform-limb and asymmetric-limb planet, which via equation 15 depends on the difference of their limb radii and the (fixed) radius of the star. To convert this difference in path length to a duration of time, we simply divide by the (fixed) orbital speed. The result is

$$\tau = \frac{\Delta x}{2v_p} \left( \frac{x}{2} \right) \cdot \frac{1}{v_p} \rightarrow \text{make it more obvious where this comes from} \quad (16)$$

*define  
 $\Delta X$*

$$= \frac{1}{2v_p} \left[ \left( R_\star - \sqrt{R_\star^2 - y_1^2} \right) - \left( R_\star - \sqrt{R_\star^2 - y_2^2} \right) \right] \quad (17)$$

$$\tau = \frac{1}{2v_p} \left[ \sqrt{R_\star^2 - y_2^2} - \sqrt{R_\star^2 - y_1^2} \right] \quad (18)$$

Here,  $y_1$  and  $y_2$  represent the polar radii of the larger and smaller hemispheres, respectively. In our case, these are the radii of the asymmetric-limb planet's morning limb and the uniform-limb planet. Therefore, we would have

$$\tau = \frac{1}{2v_p} \left[ \sqrt{R_\star^2 - R_{eff}^2} - \sqrt{R_\star^2 - R_{morning}^2} \right]. \quad (19)$$

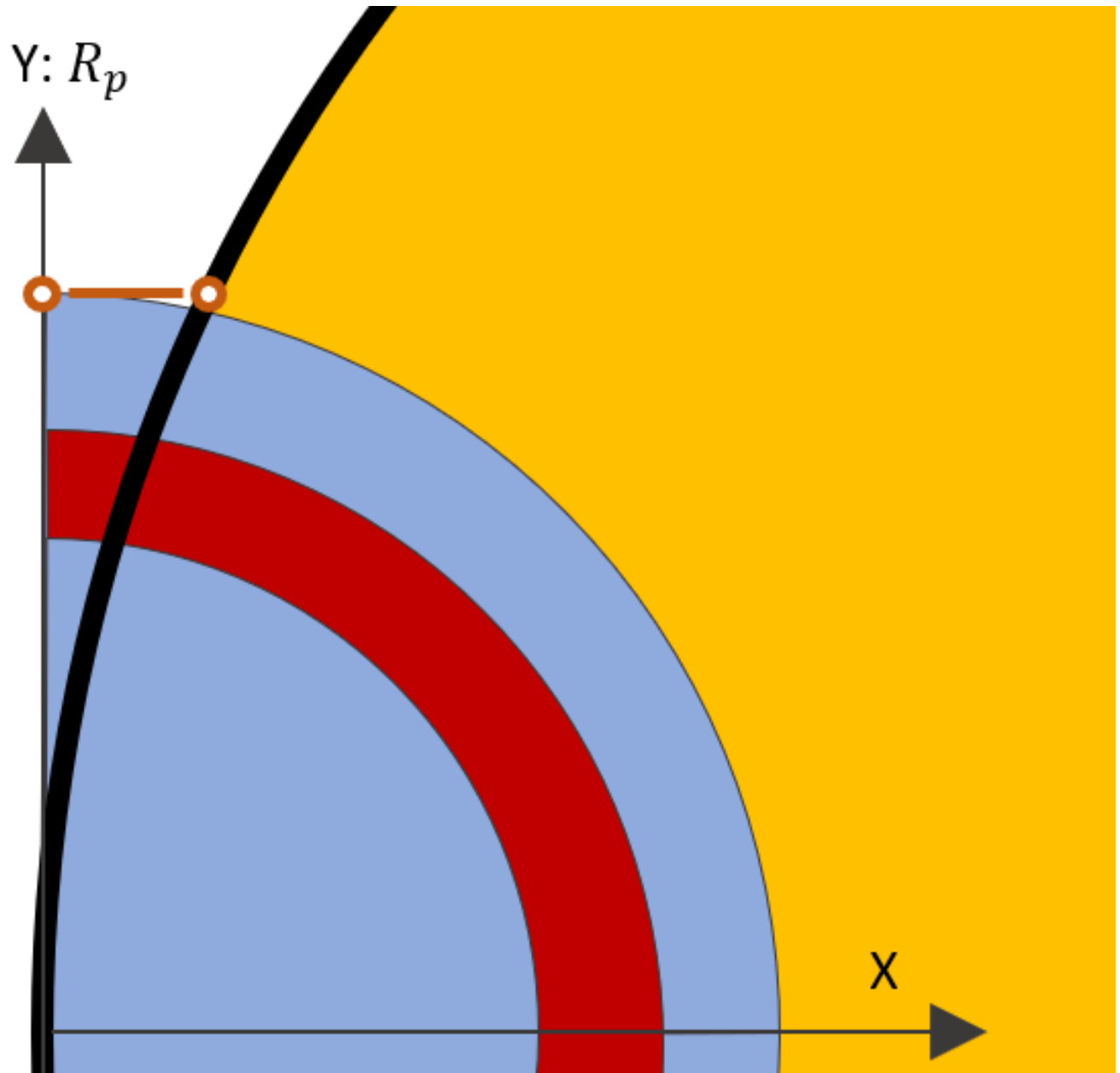


**Figure 6.** Schematic showing the extra distance necessary for a disk hemisphere to travel between the point when the whole-disk center is contacting the disk and the point when the entire hemisphere will be internally tangent. The blue and red semi-circles represent the hemispheres of our uniform-limb and asymmetric-limb planets shown in Figures 1 and 6, and the orange circle is the star. This extra distance is equal to the x-value of the stellar disk at a given y, where the y-coordinate is described by the radius of the disk hemisphere. We use this as the basis for our derivation of the extra-area compensation given by Equation 18. **Edit Note – I rotated this figure so that the x,y convention matched the other figures. I also edited all of the x,y's in the corresponding text to match this updated convention.**

We computed the expected extra-area compensation for our “perfect” observation of WASP-39b scenario using equation 19 and add it to our nominal numerical results shown in Figure 4. The result is shown as the square points which we see are now in very good agreement with our analytical model. This validates that our derived compensation  $\tau$  is indeed the difference between our analytical and numerical models. There is still a small outstanding residual between the two which seems to increase with increasing  $N$ . As alluded to previously, this is likely the result of us assuming the asymmetric-limb planet’s cross-section is composed of two connected semi-circles with discontinuity in the polar regions, as this discontinuity becomes more extreme with increasing  $N$ . We argue this additional residual is negligible though, as it reaches less than one-quarter of a second for the most extreme case of limb asymmetry. Achieving such precision on  $t_c$  is beyond the capability of current instruments, and limb asymmetry of  $N > 5$  may be unfeasible in nature anyways.

### 3.5. “Realistic” case results

Now we return to the results of our “realistic” simulated observations of WASP-80b, WASP-96b, WASP-39b, and WASP-107b described in Section 3.1. We plot the best-fit timing biases  $\Delta t_c$  as a function of  $N$  for each simulation in Figure 7, including the corresponding compensation biases from Equation 18. We compare these to the corresponding analytical model predictions for each planet from Equation 11. We see that our numerical results agree extremely well with our analytical model when accounting for the extra-area compensation. The remaining residuals are consistent — strictly speaking, you don’t know this for sure solely a result of the noise and cadence of each simulated observation.

Figure 8 shows the calculated magnitude of the numerical extra area compensation corrections for each planet. We find that the correction at any given  $N$  is larger for planets with larger atmospheric scale heights, like WASP-39b and WASP-107b. That is, this numerical overcompensation is larger when modeling a planet with a larger difference in physical radius between its limbs. Even for our most extreme case of WASP-107b, however, this magnitude of this correction is only on the order of several seconds. WASP-107b is one of the lowest density exoplanets known to date and thus has one

I'm not sure Fig 8 is worth showing. What does it say that's not in Eq 19? Fig 4  
Fig 7?

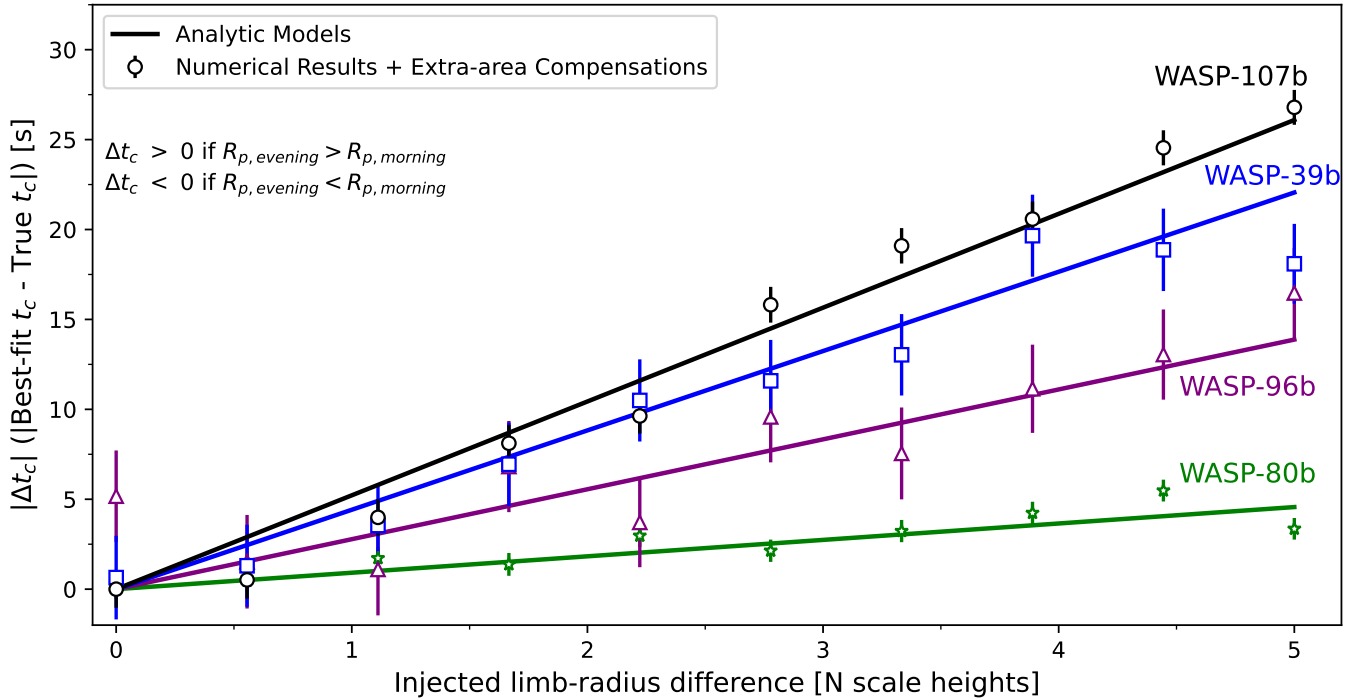


Figure 7. Measured times of conjunction compared to the truths ( $\Delta t_c$ ) as a function of the injected limb radius difference for simulated observations of representative exoplanets, including the numerical extra-area compensation effect described by Equation 18. We simulated transit data with an asymmetric-limb transit model but fit them using a uniform-limb transit model, similar to what may happen with real observations. The solid lines show our analytical model's predictions for  $\Delta t_c$  using Equation 11. We find excellent agreement between our analytical and numerical models. Our models quantify how the time of conjunction measured from a transit observation is biased if the planet has limb asymmetry but this limb asymmetry is ignored at the light curve fitting stage.

of the highest bulk scale heights of any exoplanet, so it can be taken as an upper limit for what this overcompensation would be for any general exoplanet. The range of magnitudes of limb asymmetry in nature is not known, but for a modest case of  $N = 1$  or 2 this correction is generally less than one second.

*General point: this sounds like you're worried about timing offsets in T<sub>c</sub> values. But you really care about "how well do we need to know T<sub>c</sub> to measure LA?" then write from that angle.*

#### 4. DISCUSSION

##### 4.1. Implications for literature ephemerides

*in the text too!*

*same comment*

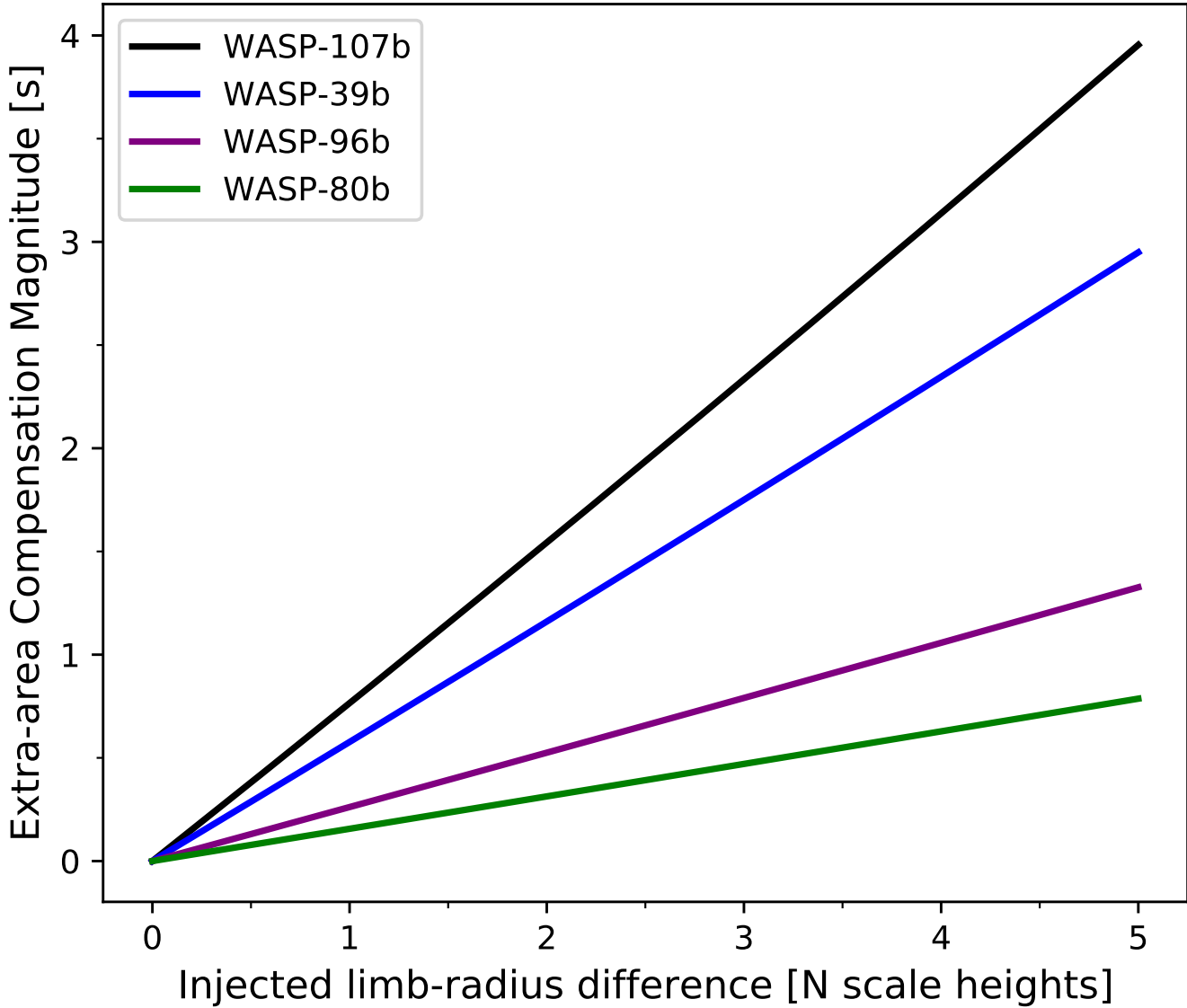


**Figure 8.** Magnitude of the numerical extra-area compensation effect as a function of limb radius difference, calculated for various representative exoplanets using Equation 18. This effect represents an additional bias in the measured time of conjunction of a planet with asymmetric limbs to what we derive in Equation 11 due to the goodness-of-fit metric optimization method used by numerical fitting techniques. For limb asymmetry of a few scale heights difference between limb radii, this compensation is on the order of one second. We find that planets with higher atmospheric scale heights have larger compensations for a given degree of limb asymmetry, as the slopes of the lines shown here increase in order of increasing scale height.

340

The majority of, if not all, measurements of exoplanet transit times in the literature result from fitting data using a uniform-limb transit model. An immediate implication of this is that if any of

341

*Let's talk about the discussion*

these planets have limb asymmetry, these literature measurements are biased, particularly if they only used observations in a single bandpass. As we have shown, even for moderate limb asymmetry these literature times of conjunction may be biased by several to tens of seconds due purely to the planet's limb asymmetry, as well as an additional couple seconds of bias due to the numerical extra-area compensation effect. In all cases, we find that the physical bias in the time of conjunction due to limb asymmetry is larger than the numerical extra-area compensation effect. These biases are exaggerated for planets with high atmospheric scale heights, though this may actually work in their favor as, in these cases, it may be easier to measure the transit times with uncertainty smaller than the expected bias using multi-wavelength observations.

Our work here assumes having just a single light curve, such as a band-integrated observation, which underscores the potential danger in relying on a single-band observation for measuring a precise time of conjunction if interested in investigating limb asymmetry. Other works in the literature have discussed the utility of instead using a multi-wavelength approach (e.g. Powell et al. 2019), where the different spectral variations of each limb's radius compared to having a single, non-wavelength dependent time of conjunction reduces the strength of their degeneracy. Even if this physical bias is eliminated, however, fits of the time of conjunction may still be biased by the numerical extra-area compensation effect. Although this effect is relatively small, it will be relevant for very high-precision times, with uncertainties less than one second, that are currently possible with combined JWST observations (e.g. Murphy & et al. 2023b, in review; Carter & et al. 2023, in review). We recommend always considering all potential biases when using a literature transit time for an analysis of limb asymmetry.

#### 4.2. *Limitations of the semi-circle cross-section model*

As mentioned previously, the semi-circle based model that we use for our asymmetric-limb planetary disk, both when deriving our analytic model and when using catwoman in our numerical model, is not strictly realistic. As seen clearly in the exaggerated example in Figure 1, this construction creates a discontinuity in the atmosphere near the planet's poles, which becomes more extreme for greater limb asymmetry. This

369 limitation, however, is unlikely to be important given current and near-future data  
370 quality. For example, as seen in the square-point residuals in Figure 4 and discussed  
371 in Section 3.4, this discontinuity only induces error in our model of approximately one  
372 tenth of a second for limb asymmetry greater than five scale heights. While this was  
373 calculated just for one example exoplanet, the magnitude would not be significantly  
374 different for other planets. Transit timing at such high precision is likely not achievable  
375 with current instrumentation, as combined fits of state-of-the-art JWST, TESS, Spitzer,  
376 and ground-based data have only been able to achieve  $1-\sigma$  uncertainty on  $t_c$  of  $\sim 0.6$  s  
377 or worse. Also, it is not clear from current observations whether limb asymmetry as  
378 large as five scale heights and greater actually exists in nature. Nevertheless, analytic  
379 and numerical models which define fully continuous atmospheric surfaces, such as the  
380 transmission string numerical model (Grant & Wakeford 2023), may improve upon our  
381 result.

#### 382 4.3. Additional effects on the observability of limb asymmetry

383 Some exoplanets exhibit transit timing variations (TTVs) induced by gravitational interaction  
384 with other planets in the same system (e.g. Maciejewski et al. 2010; Adams et al. 2011). The  
385 amplitude of these TTVs can range from less than one second to tens of minutes depending on the  
386 orbital architecture of the system, and have variation periods upwards of hundreds of years. For  
387 certain planets, these TTVs may place a limit on the achievable precision on a planet’s time of  
388 conjunction that is comparable or worse than the timing biases derived here. Therefore, unless the  
389 underlying TTV trend is known extremely well, it will likely be difficult to disentangle signatures of  
390 limb asymmetry from the uncertainty in the time of conjunction generated by TTV interactions for  
391 such planets.

392 Stellar surfaces are not perfectly homogeneous, and many exoplanet-hosting stars are known to  
393 have starspots and faculae on their surfaces. These stellar surface heterogeneities influence the signal  
394 observed during a planet’s transit, which can lead to biased inferences of the planet’s atmosphere if not  
395 properly accounted for (e.g. Rackham et al. 2018, 2019; Barclay et al. 2021; Moran et al. 2023). We did

396 not consider the impact of stellar surface heterogeneities in this work and always assumed uniformly  
397 bright stellar disks. Our results apply most directly to scenarios when any stellar contamination can  
398 be confidently ruled out or modeled. A more detailed study is warranted to examine how stellar  
399 contamination could further mimic or bias inferences of exoplanet limb asymmetry.

400 Finally, our analysis constructed the disk of an asymmetric-limb planet by explicitly assuming  
401 east-west asymmetry where each hemisphere is a uniform semi-circle. Real exoplanet atmospheres  
402 are likely not this ideal. For example, strong meridional circulation that preferentially transports  
403 condensates to a planet's polar regions may cause pole-equator asymmetry that is more significant  
404 than east-west asymmetry (e.g. see Parmentier et al. 2013; Charnay et al. 2015; Line & Parmentier  
405 2016). In this case, the planetary disk would be shaped differently than we have assumed, either as  
406 a 90-degree rotation or even a non-semi-circular shape, which would likely lead to a different form of  
407 the limb asymmetry - transit timing degeneracy than we have derived here.

## 408 5. SUMMARY

409 Measuring morning-to-evening variations of temperature, elemental and molecular abundances, and  
410 aerosol properties in exoplanet atmospheres is critical to understanding the underlying circulation  
411 and dynamics of the atmosphere. Transit observations are able to extract the separate contributions  
412 from a planet's morning and evening terminator using high-resolution ground-based spectroscopy  
413 and, more recently, low-resolution space-based spectroscopy with JWST. Particularly for the latter,  
414 a strong degeneracy exists between the effect of limb asymmetry on a light curve and uncertainty in  
415 the planet's time of conjunction. In this work, we have described the origin of this degeneracy and  
416 derived an analytical formula for it, given in Equation 11. We find that limb asymmetry of one to two  
417 scale heights difference in limb radii can cause upwards of ten seconds in bias to the measured time  
418 of conjunction. Further, we find that this bias is more extreme for planets with larger scale height.  
419 **When comparing our analytical framework to simulated observations of an asymmetric-**  
420 **limb planet fit using a uniform-limb model, we find that there is an additional bias**  
421 **to the inferred time of conjunction from these observations due to the goodness-of-fit**  
422 **metric used by numerical techniques. This bias can be of the order of a couple seconds**

for moderate limb asymmetries. We dub this the “extra-area compensation effect” as it stems from the relative occulting areas of a uniform-limb disk and asymmetric-limb disk when stacked atop one another, and derive an analytical formula for it as well in Equation 18. Since we used the same numerical techniques as are used in practice for analyzing real transit observations, this additional bias is likely present in literature transit times.

The authors would like to acknowledge Kevin Hardegree-Ullman, Megan Mansfield, and Everett Schlawin for helpful discussions that inspired this study. M.M.M. acknowledges funding from NASA Goddard Spaceflight Center via NASA contract NAS5-02105. This material is based upon work supported by the National Aeronautics and Space Administration under Agreement No. 80NSSC21K0593 for the program “Alien Earths”. The results reported herein benefited from collaborations and/or information exchange within NASA’s Nexus for Exoplanet System Science (NExSS) research coordination network sponsored by NASA’s Science Mission Directorate.

*Facilities:* Exoplanet Archive

*Software:* batman (Kreidberg 2015), catwoman (Jones & Espinoza 2022; Espinoza & Jones 2021b), emcee (Foreman-Mackey et al. 2013), matplotlib (Hunter 2007), NumPy (Harris et al. 2020), PandExo (Batalha et al. 2017), SciPy (Virtanen et al. 2020)

## REFERENCES

- |   |  |
|---|--|
| <p>440 Adams, E. R., López-Morales, M., Elliot, J. L.,<br/>         441 Seager, S., &amp; Osip, D. J. 2011, ApJ, 728, 125,<br/>         442 doi: <a href="https://doi.org/10.1088/0004-637X/728/2/125">10.1088/0004-637X/728/2/125</a></p> <p>443 Anderson, D. R., Collier Cameron, A., Delrez, L.,<br/>         444 et al. 2017, A&amp;A, 604, A110,<br/>         445 doi: <a href="https://doi.org/10.1051/0004-6361/201730439">10.1051/0004-6361/201730439</a></p> <p>446 Apai, D., Karalidi, T., Marley, M. S., et al. 2017,<br/>         447 Science, 357, 683, doi: <a href="https://doi.org/10.1126/science.aam9848">10.1126/science.aam9848</a></p> | <p>448 Barclay, T., Kostov, V. B., Colón, K. D., et al.<br/>         449 2021, AJ, 162, 300,<br/>         450 doi: <a href="https://doi.org/10.3847/1538-3881/ac2824">10.3847/1538-3881/ac2824</a></p> <p>451 Batalha, N. E., Mandell, A., Pontoppidan, K.,<br/>         452 et al. 2017, PASP, 129, 064501,<br/>         453 doi: <a href="https://doi.org/10.1088/1538-3873/aa65b0">10.1088/1538-3873/aa65b0</a></p> |
|---|--|

- 454 Beatty, T. G., Marley, M. S., Gaudi, B. S., et al.  
 455 2019, AJ, 158, 166,  
 456 doi: [10.3847/1538-3881/ab33fc](https://doi.org/10.3847/1538-3881/ab33fc)
- 457 Bonomo, A. S., Desidera, S., Benatti, S., et al.  
 458 2017, A&A, 602, A107,  
 459 doi: [10.1051/0004-6361/201629882](https://doi.org/10.1051/0004-6361/201629882)
- 460 Borsa, F., Allart, R., Casasayas-Barris, N., et al.  
 461 2021, A&A, 645, A24,  
 462 doi: [10.1051/0004-6361/202039344](https://doi.org/10.1051/0004-6361/202039344)
- 463 Bourrier, V., Ehrenreich, D., Lendl, M., et al.  
 464 2020, A&A, 635, A205,  
 465 doi: [10.1051/0004-6361/201936640](https://doi.org/10.1051/0004-6361/201936640)
- 466 Buenzli, E., Marley, M. S., Apai, D., & Lupu,  
 467 R. E. 2014, Cloud structure of brown dwarfs  
 468 from spectroscopic variability observations.  
 469 <https://arxiv.org/abs/1406.0210>
- 470 Caldas, A., Leconte, J., Selsis, F., et al. 2019,  
 471 A&A, 623, A161,  
 472 doi: [10.1051/0004-6361/201834384](https://doi.org/10.1051/0004-6361/201834384)
- 473 Carter, A.L., M. E., & et al. 2023, in review
- 474 Charnay, B., Meadows, V., Misra, A., Leconte, J.,  
 475 & Arney, G. 2015, ApJL, 813, L1,  
 476 doi: [10.1088/2041-8205/813/1/L1](https://doi.org/10.1088/2041-8205/813/1/L1)
- 477 Dai, F., & Winn, J. N. 2017, AJ, 153, 205,  
 478 doi: [10.3847/1538-3881/aa65d1](https://doi.org/10.3847/1538-3881/aa65d1)
- 479 Delisle, S., & et al. 2023, in review
- 480 Ehrenreich, D., Lovis, C., Allart, R., et al. 2020,  
 481 Nature, 580, 597,  
 482 doi: [10.1038/s41586-020-2107-1](https://doi.org/10.1038/s41586-020-2107-1)
- 483 Espinoza, N., & et al. 2023, in review
- 484 Espinoza, N., & Jones, K. 2021a, AJ, 162, 165,  
 485 doi: [10.3847/1538-3881/ac134d](https://doi.org/10.3847/1538-3881/ac134d)
- 486 —. 2021b, AJ, 162, 165,  
 487 doi: [10.3847/1538-3881/ac134d](https://doi.org/10.3847/1538-3881/ac134d)
- 488 Faedi, F., Barros, S. C. C., Anderson, D. R., et al.  
 489 2011, A&A, 531, A40,  
 490 doi: [10.1051/0004-6361/201116671](https://doi.org/10.1051/0004-6361/201116671)
- 491 Feinstein, A. D., Radica, M., Welbanks, L., et al.  
 492 2022, arXiv e-prints, arXiv:2211.10493,  
 493 doi: [10.48550/arXiv.2211.10493](https://doi.org/10.48550/arXiv.2211.10493)
- 494 Feng, Y. K., Line, M. R., Fortney, J. J., et al.  
 495 2016, ApJ, 829, 52,  
 496 doi: [10.3847/0004-637X/829/1/52](https://doi.org/10.3847/0004-637X/829/1/52)
- 497 Fischer, P. D., Knutson, H. A., Sing, D. K., et al.  
 498 2016, ApJ, 827, 19,  
 499 doi: [10.3847/0004-637X/827/1/19](https://doi.org/10.3847/0004-637X/827/1/19)
- 500 Foreman-Mackey, D., Hogg, D. W., Lang, D., &  
 501 Goodman, J. 2013, PASP, 125, 306,  
 502 doi: [10.1086/670067](https://doi.org/10.1086/670067)
- 503 Gaia Collaboration, Brown, A. G. A., Vallenari,  
 504 A., et al. 2018, A&A, 616, A1,  
 505 doi: [10.1051/0004-6361/201833051](https://doi.org/10.1051/0004-6361/201833051)
- 506 Grant, D., & Wakeford, H. R. 2023, MNRAS, 519,  
 507 5114, doi: [10.1093/mnras/stac3632](https://doi.org/10.1093/mnras/stac3632)
- 508 Harris, C. R., Millman, K. J., van der Walt, S. J.,  
 509 et al. 2020, Nature, 585, 357,  
 510 doi: [10.1038/s41586-020-2649-2](https://doi.org/10.1038/s41586-020-2649-2)
- 511 Hellier, C., Anderson, D. R., Collier Cameron, A.,  
 512 et al. 2014, MNRAS, 440, 1982,  
 513 doi: [10.1093/mnras/stu410](https://doi.org/10.1093/mnras/stu410)
- 514 Hoeijmakers, H. J., Cabot, S. H. C., Zhao, L.,  
 515 et al. 2020, A&A, 641, A120,  
 516 doi: [10.1051/0004-6361/202037437](https://doi.org/10.1051/0004-6361/202037437)

- 517 Hunter, J. D. 2007, Computing in Science &  
 518 Engineering, 9, 90, doi: [10.1109/MCSE.2007.55](https://doi.org/10.1109/MCSE.2007.55)
- 519 Jones, K., & Espinoza, N. 2022, Journal of Open  
 520 Source Software, 7, 2382,  
 521 doi: [10.21105/joss.02382](https://doi.org/10.21105/joss.02382)
- 522 Kataria, T., Sing, D. K., Lewis, N. K., et al. 2016,  
 523 ApJ, 821, 9, doi: [10.3847/0004-637X/821/1/9](https://doi.org/10.3847/0004-637X/821/1/9)
- 524 Kesseli, A. Y., & Snellen, I. A. G. 2021, ApJL,  
 525 908, L17, doi: [10.3847/2041-8213/abe047](https://doi.org/10.3847/2041-8213/abe047)
- 526 Kokori, A., Tsiaras, A., Edwards, B., et al. 2022,  
 527 ApJS, 258, 40, doi: [10.3847/1538-4365/ac3a10](https://doi.org/10.3847/1538-4365/ac3a10)
- 528 Kreidberg, L. 2015, PASP, 127, 1161,  
 529 doi: [10.1086/683602](https://doi.org/10.1086/683602)
- 530 Line, M. R., & Parmentier, V. 2016, ApJ, 820, 78,  
 531 doi: [10.3847/0004-637X/820/1/78](https://doi.org/10.3847/0004-637X/820/1/78)
- 532 Maciejewski, G., Dimitrov, D., Neuhäuser, R.,  
 533 et al. 2010, MNRAS, 407, 2625,  
 534 doi: [10.1111/j.1365-2966.2010.17099.x](https://doi.org/10.1111/j.1365-2966.2010.17099.x)
- 535 Maciejewski, G., Dimitrov, D., Mancini, L., et al.  
 536 2016, AcA, 66, 55.  
 537 <https://arxiv.org/abs/1603.03268>
- 538 Mancini, L., Esposito, M., Covino, E., et al. 2018,  
 539 A&A, 613, A41,  
 540 doi: [10.1051/0004-6361/201732234](https://doi.org/10.1051/0004-6361/201732234)
- 541 May, E. M., Stevenson, K. B., Bean, J. L., et al.  
 542 2022, AJ, 163, 256,  
 543 doi: [10.3847/1538-3881/ac6261](https://doi.org/10.3847/1538-3881/ac6261)
- 544 Metchev, S. A., Heinze, A., Apai, D., et al. 2015,  
 545 The Astrophysical Journal, 799, 154,  
 546 doi: [10.1088/0004-637x/799/2/154](https://doi.org/10.1088/0004-637x/799/2/154)
- 547 Moran, S. E., Stevenson, K. B., Sing, D. K., et al.  
 548 2023, High Tide or Riptide on the Cosmic  
 549 Shoreline? A Water-Rich Atmosphere or Stellar  
 550 Contamination for the Warm Super-Earth  
 551 GJ 486b from JWST Observations.  
 552 <https://arxiv.org/abs/2305.00868>
- 553 Murphy, M., & et al. 2023b, in review
- 554 Parmentier, V., Showman, A. P., & Lian, Y. 2013,  
 555 A&A, 558, A91,  
 556 doi: [10.1051/0004-6361/201321132](https://doi.org/10.1051/0004-6361/201321132)
- 557 Patel, J. A., & Espinoza, N. 2022, AJ, 163, 228,  
 558 doi: [10.3847/1538-3881/ac5f55](https://doi.org/10.3847/1538-3881/ac5f55)
- 559 Piaulet, C., Benneke, B., Rubenzahl, R. A., et al.  
 560 2021, AJ, 161, 70,  
 561 doi: [10.3847/1538-3881/abcd3c](https://doi.org/10.3847/1538-3881/abcd3c)
- 562 Powell, D., Louden, T., Kreidberg, L., et al. 2019,  
 563 ApJ, 887, 170, doi: [10.3847/1538-4357/ab55d9](https://doi.org/10.3847/1538-4357/ab55d9)
- 564 Rackham, B. V., Apai, D., & Giampapa, M. S.  
 565 2018, ApJ, 853, 122,  
 566 doi: [10.3847/1538-4357/aaa08c](https://doi.org/10.3847/1538-4357/aaa08c)
- 567 —. 2019, AJ, 157, 96,  
 568 doi: [10.3847/1538-3881/aaf892](https://doi.org/10.3847/1538-3881/aaf892)
- 569 Rustamkulov, Z., Sing, D. K., Mukherjee, S.,  
 570 et al. 2022, arXiv e-prints, arXiv:2211.10487,  
 571 doi: [10.48550/arXiv.2211.10487](https://doi.org/10.48550/arXiv.2211.10487)
- 572 Taylor, J., Parmentier, V., Irwin, P. G. J., et al.  
 573 2020, MNRAS, 493, 4342,  
 574 doi: [10.1093/mnras/staa552](https://doi.org/10.1093/mnras/staa552)
- 575 Triaud, A. H. M. J., Gillon, M., Ehrenreich, D.,  
 576 et al. 2015, MNRAS, 450, 2279,  
 577 doi: [10.1093/mnras/stv706](https://doi.org/10.1093/mnras/stv706)

578 Virtanen, P., Gommers, R., Oliphant, T. E., et al.

579 2020, *Nature Methods*, 17, 261,

580 doi: [10.1038/s41592-019-0686-2](https://doi.org/10.1038/s41592-019-0686-2)

581 von Paris, P., Gratier, P., Bordé, P., Leconte, J.,

582 & Selsis, F. 2016, *A&A*, 589, A52,

583 doi: [10.1051/0004-6361/201527894](https://doi.org/10.1051/0004-6361/201527894)